2019 International Conference on Robotics and Automation (ICRA)
Palais des congres de Montreal, Montreal, Canada, May 20-24, 2019

Toward Fingertip Non-Contact Material Recognition and Near-Distance Ranging for Robotic Grasping*

Cheng Fang, Di Wang, Dezhen Song, and Jun Zou

Abstract— **We report the feasibility study of a new acoustic and optical bi-modal distance & material sensor for robotic grasping. The new sensor is designed to be mounted on the robot fingertip to provide last-moment perception before contact happens. It is based on both pulse-echo ultrasound and optoacoustic effects enabled by single-element air-coupled transducers. In contrast to conventional contact-based and recent pre-touch approaches, this new method overcomes their disadvantages and provides robotic fingers with the capability to detect the distance and material type of the target at a near distance before contact occurs, which is crucial for robust and nimble grasping. The proposed sensor has been tested with different materials, shapes, and porous properties. The experimental results show that this sensor design is functional and practical.**

I. Introduction

Achieving reliable grasping has been a grand challenge for robotics researchers [1] [2]. Grasping dictates how a robot can interact with physical objects and inherently determines the tasks that the robot can perform. Sensor-less grasping exists but suffers from efficiency issues [3] [4]. A normal grasping procedure following a standard sense-plan-act (SPA) methodology suffers from unreliable and incomplete sensing. A good sensor for grasping should be able to detect object relative pose at near distance and recognize material type of the object if possible. The near distance ranging (< 0.5 cm) is important because it allows the robot to dynamically and precisely respond to subtle changes in object pose right before the grasping operation and adjust operations dynamically during grasping. The material type information can help planner to estimate impact characteristic and friction coefficients for better grasping.

Existing sensors and perception algorithms have difficulties in satisfying these requirements. A camera can observe the physical object at a distance but often cannot obtain precise relative pose due to the occlusion caused by closing-in fingers themselves [5]. LIDARs have been successfully applied for robotic mapping and navigation [6] [7] and can achieve millimeter-level resolution [8]. However, a LIDAR measures distance using time-of-flight and has a blind zone when the perceived object is too close. Radar ranging is mainly applied for long distance detection with the optimal resolution of several centimeters [9]. Similar to LIDARs, a radar also has blind zone for near-distance ranging. Optical and E-field proximity sensors have been developed for pre-touch ranging recently, but the optical sensors work not well for transparent or highly reflective targets [10] [11], and the E-field sensors have difficulties in detecting materials with low dielectric contrast to air, such as fabrics, thin plastics, and thin sheets of paper [12] [13]. Ultrasonic ranging can measure near distance [14] [15] [16] but has limited lateral resolution due to its widespread signal dispersion pattern. Another possible approach is to employ tactile sensing [17] [18] or force sensing [19]. However, tactile and force sensing requires the robot to touch the object which may change object poses or even damage the object. It leads to either slow grasping process or complete failure in grasping.

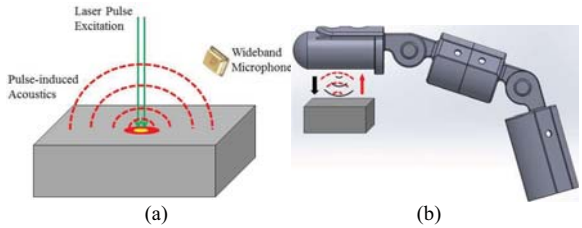

Figure 1. (a) A diagram of laser pulse-induced (ultra)sound (optoacoustics). (b) A simplified diagram of robotic finger transmitting sound / laser beams (in black) onto target and receiving reflected / induced sound waves (in red). We add our sensor to the finger design in [27] to illustrate the idea.

To address these issues, this paper reports the initial study of a new bi-modal acoustic and optical distance & material sensor for robotic grasping which combines optoacoustic effect (Fig. 1(a)) for material sensing and ultrasonic ranging into a single finger-mounted device (see Fig. 1(b)). In contrast to conventional contact-based and recent pre-touch approaches, this new method overcomes their disadvantages and provides robotic fingers with the capability to detect the distance and material type of the target at a close distance before contact occurs. For material recognition, we employ both pulse-echo ultrasound and optoacoustic approaches. The pulse-echo ultrasound measures the distance but may have issues in (dense) material differentiation. For the latter, the optoacoustic approach employs a modulated short laser pulse to induce ultrasound wave for material differentiation according to frequency responses. The proposed approach has been tested on seven different materials and the initial results are promising.

For distance ranging, we integrate a parabolic mirror inside the robot finger to allow a focused ultrasound beam to improve spatial resolution. The maximum distance error is less than 0.23 mm. For the lateral resolution, the FWHM (full-width at half-maximum) is 0.57 mm. We have also tested the distance ranging under different shapes and profiles. Our results show that the pulse-echo ultrasound distance ranging is

*The research is supported in part by National Science Foundation under NRI-1748161 and NRI-1526200.

C. Fang and J. Zou are with the Electrical and Computer Engineering Department, Texas A&M University, College Station, TX 77843, USA (e-mails: {fangchengok2007, junzou}@tamu.edu).

D. Wang and D. Song are with the Computer Science and Engineering Department, Texas A&M University, College Station, TX 77843, USA (e-mails: ivanwang@tamu.edu, dzsong@cs.tamu.edu).

not sensitive to the shape, area, and profile of targets, because similar reflected pulse has been received from each element, despite some differences in amplitude.

II. Principles and Methods

A. Distance Ranging by Pulse-echo Ultrasound

Fig. 2 shows the principle of ultrasound distance sensing [20]. Due to the mismatch in their acoustic impedance, the ultrasound pulse sent by the transducer will be reflected at the air-target interface. The time delay (t) between the transmitted pulse and the reflected signal ("echo") is equal to the travel time of a round trip between the transducer and the target. Therefore, the distance between the transducer and the target can be determined by

$$L = ct/2, \tag{1}$$

where c is the sound velocity in air, which is ~340 m/s.

Because the sound velocity can be considered as constant within the (small) distance between the transducer and the target, the distance ranging resolution is mainly affected by the accuracy in the travel time estimation, which is in turn impacted by the ultrasound frequency. The smooth low-frequency ultrasound signal makes its starting point unclear out of the background waveform. To estimate the delay (t) more accurately, the transducer needs to operate at higher frequencies to make the signal starting point more clear, based on the sharp waveform change over background. A second benefit of higher frequency is the smaller focal spot size (φ), leading to a good lateral resolution for identifying smaller objects, which is estimated by

$$\varphi = 2.44 \cdot \left(\frac{l_f}{D}\right) \cdot \frac{c}{f}, \tag{2}$$

where l_f is the focal length, D is the transducer diameter, c is the sound velocity, and f is the operation frequency [20]. However, the acoustic attenuation in air increases drastically with frequency [21], thereby reducing the detectable range. For 1 MHz ultrasound, the acoustic attenuation (α) in air is ~1.6 dB/cm [22]. In this work, an operation frequency of 1 MHz is chosen to provide a good balance of resolution and working range.

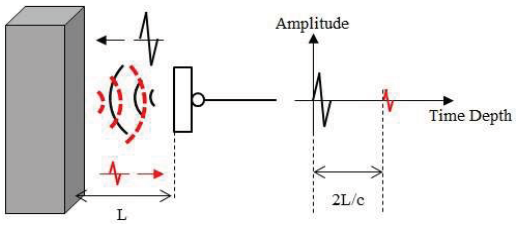

Figure 2. A diagram of the ultrasound distance ranging based on the time delay between the transmitted pulse (in black) and the received echo (in red).

B. Materials Differentiation by Pulse-echo Ultrasound

Besides distance ranging, the pulse-echo ultrasound could be used to differentiate the type of the target material based on their different acoustic reflectivity (R), which can be determined by

$$R = \frac{Z_{target} - Z_{air}}{Z_{target} + Z_{air}}, \tag{3}$$

where Z_{target} and Z_{air} are the acoustic impedances of the target material and air, respectively. The acoustic impedance (Z) of a material could be calculated as

$$Z = \rho c = \rho \cdot \sqrt{\frac{E}{\rho}} = \sqrt{\rho E} \tag{4}$$

where ρ is the density, c is the sound velocity, and E is the Young's modulus of the target material.

The acoustic impedances of some common materials in robotic grasping are listed in Table I. According to equation (3), the reflectivity follows

$$R_{Foam} < R_{Paper} < R_{Rubber} \approx R_{Acrylic} \approx R_{Steel},$$

leading to the same comparison of reflection amplitudes. Therefore, the high-porosity foam, the low-porosity paper and non-porosity solids could be differentiated from their different reflection coefficients.

However, one limitation of this pulse-echo ultrasound method is that it is difficult to differentiate dense solid materials (including rubber, acrylic, steel and PZT (lead zirconate titanate)) due to their similar acoustic reflection coefficients in air.

TABLE I. Density, Acoustic Velocity, and Acoustic Impedance of Common Materials

Materials	*Density ρ(kg/m³)*	*Acoustic Velocity c (m/s)*	*Acoustic Impedance Z(MRayls)*	*Calculated Reflectivity R*
Air	1.225	343	0.00042	0
Foam Plastic (Styrofoam)	11~32 [28]	500 [29]	0.0055~0.016	0.858~0.949
Paper (Porous Cellulose)	250~1500 [30]	NA	0.08~0.56 [26]	0.990~0.999
Rubber	910~1200 [31]	1800	1.638~2.16	~1
Acrylic	1180	2730	3.22	~1
Steel	8050	5800	46.69	~1
PZT	7600	4560	34.65	~1

C. Materials Differentiation by Optoacoustics

To overcome the limitation of pulse-echo ultrasound in target material differentiation, an optoacoustic method is employed to differentiate dense solid materials based on their different response of laser-induced ultrasound. As shown in Fig. 1(a), when a short laser pulse is incident on the target surface, part of its energy is absorbed and converted into a heat pulse. The heat pulse will create a fast transient temperature rising, thermal expansion and contraction, which induces an ultrasound wave, called optoacoustic wave. The frequency spectrum of the optoacoustic wave is mainly affected by density (ρ), Young's modulus (E, describing solid stiffness), thermal expansion coefficient (α, describing solid size change with temperature) and specific heat capacity (C_p, describing temperature change with absorbed heat). A material with a higher Young's modulus / density (phase velocity $c = \sqrt{\frac{E}{\rho}}$) but a smaller thermal expansion coefficient / heat capacity (deformation $\propto \frac{\alpha}{C_p}$) can restore its shape more quickly and

therefore tend to generate a smaller period of vibration and higher acoustic frequency components [23]. Table II lists these parameters of some common dense solid materials (rubber, acrylic and steel), showing

$$\frac{\alpha_{steel}}{C_{p\_steel}} < \frac{\alpha_{acrylic}}{C_{p\_acrylic}} \approx \frac{\alpha_{rubber}}{C_{p\_rubber}}$$

and

$$\frac{E_{steel}}{\rho_{steel}} \gg \frac{E_{acrylic}}{\rho_{acrylic}} \gg \frac{E_{rubber}}{\rho_{rubber}}.$$

Therefore, when excited by laser pulses, they are expected to provide different acoustic responses, which can be detected with a wideband microphone or transducer. This forms the foundation for differentiating dense solid materials with the optoacoustic method.

TABLE II. DENSITY, YOUNG'S MODULUS, THERMAL EXPANSION COEFFICIENT AND HEAT CAPACITY OF COMMON DENSE SOLID MATERIALS

Materials	***Density* ρ(kg/m^3)**	***Young's Modulus* E (GPa) [32]**	***Thermal Expansion Coefficient* α (10^{-6} (m/(m K))) [33]**	***Specific Heat Capacity* C_p (J/(kg • K))**
Rubber	910~1200 [31]	0.01~0.1	80	1880 [34]
Acrylic	1180	3.2	68~75	1460~2160 [35]
Steel	8050	180~200	11~12.5	490 [34]

D. Optoacoustics Classification by Algorithm

The optoacoustics classification is performed with a general purpose time series classifier, Bag-of-SFA-Symbols (BOSS) [24], with high accuracy and low time complexity [25]. BOSS feature is used on the top of a 1-nearest-neighbor (1-NN) classifier. Feature obtaining has three major steps: firstly, a fixed size sliding window converts input sequence into a group of slices; secondly, Symbolic Fourier Approximation (SFA) transforms the slices into a set of symbols; finally, a histogram of the symbols is generated to represent the sequence. For classification, the 1-NN classifier compares the histogram of input sequence with existing ones, and then exports the label of sequence with the most similar histogram. Parameter search used by the ensemble version of BOSS classifier gets an optimal window size and SFA symbol length, making it parameter tuning free. The BOSS classifier is robust to noise and free from sequence alignment. Therefore, it's an ideal algorithm to classify the optoacoustic signals and validate the feasibility of materials differentiation by optoacoustics.

III. SENSOR DESIGN

Now let us explain how we integrate both ultrasound pulse-echo and optoacoustic approaches into a single fingertip sensing device. A detailed configuration of the bi-modal acoustic and optical distance & material sensor added to robotic finger is illustrated in Fig. 3. Laser pulses travelling through a hollow or transparent air-coupled transducer are to be reflected and focused by a parabolic mirror onto target to induce the optoacoustic wave. A small wideband microphone is added to the finger tip to receive the laser-induced sound for dense material recognition. Besides the optoacoustic modality, ultrasound pulses are transmitted from transducer and directed onto target by the parabolic mirror. The ultrasound pulses reflected from air-target interface propagate along the reversal path to be received by transducer, for near-distance ranging and porous material recognition.

A metal-coated PZT substrate (STEINER & MARTINS, INC., Doral, FL) has been prepared to make the air-coupled transducer (Fig. 4). The thickness of the PZT substrate is 2 mm to provide a fundamental resonance frequency around 1 MHz. Conductive epoxy (E-Solder® 3022, Von Roll, New Haven, CT) has been applied onto the back surface of the PZT substrate as a backing material to damp the self-resonance. A ~0.7 mm thick epoxy (Epotek 301, Epoxy Technology, Inc., Billerica, MA) has been applied onto the front surface as an acoustic impedance matching layer to improve the coupling efficiency of the acoustic energy between PZT and air. A 50-ohm micro co-axial cable (No. 141118-02, Wellshow Technology, Taiwan) has been soldered onto the PZT substrate for electrical connection.

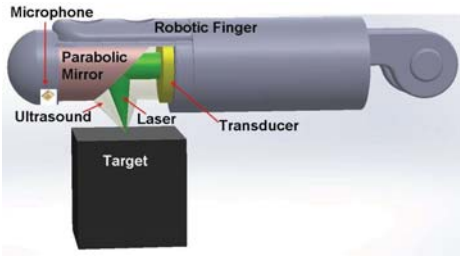

Figure 3. A diagram of bi-modal acoustic and optical distance & material sensor added to robotic finger.

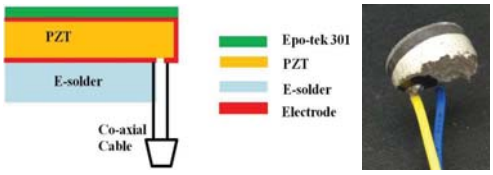

Figure 4. (a) Schematic of air-coupled PZT ultrasound transducer. (b) Photograph of the fabricated air-coupled PZT ultrasound transducer.

IV. EXPERIMENTS AND RESULTS

A. Ultrasound Distance Ranging

The setup of ultrasound distance ranging is shown in Fig. 5 (a). The air-coupled PZT transducer and the parabolic mirror have been assembled together into a custom-designed and 3D-printed fixture (Fig. 5 (b)). The transducer has been driven by a pulser-receiver (5072PR, Olympus NDT, Waltham, MA, USA) with a 5 kHz pulse repetition rate. The transmitted ultrasound pulses have been reflected and focused by a 90° aluminum parabolic mirror (35-481, 12.7 × 12.7 mm EFL, Edmund Optics, Barrington, NJ, USA) with a travel distance of $L_1 + L_2 + d$. The reflected pulses propagate along the reversal path, and are received by the transducer and amplified by the preamplifier embedded in pulser-receiver. The amplified signals have been captured and recorded with a digital oscilloscope (TDS2014C, Tektronix Inc., Beaverton, OR, USA) at a sampling rate of 10 MHz. A steel block with a flat surface mounted onto an adjustable Z-axis stage has been

used as the testing target. The distance (d) between the parabolic mirror and the steel block has been decreased from 5 mm to 0 with a decrement of 0.5 mm. At each distance, before the round-trip delay is determined, the pulse-echo cycle has been repeated 128 times to average the recorded signals for improving the signal-to-noise ratio (SNR).

Fig. 6 shows a captured ultrasound pulse-echo signal, indicating the measured delay between the "pulse" and "echo" for distance calculation. Fig. 7 (a) shows the delay-calculated distance vs. the real distance (d) from 5 mm to 0. Fig. 7 (b) shows the deviations of the delay-calculated distance from the real one. When the target is close to the focal point (d = 5 mm), the ultrasound wave reflects and arrives at almost the same time, resulting in the smallest deviation and highest accuracy in the delay-calculated distance. Therefore, the delay at distance (d) of 5 mm has been set as the reference for evaluating the deviation at other distances. When the target moves away from the focal point and even outside the focal zone (when d is up to centimeters or close to 0 mm), the asynchronous arrival of ultrasound wave leads to larger deviation and lower accuracy of distance estimation. The deviation is smaller than 0.1 mm when target is within or close to the focal zone (when d ranging from 5 mm to 2 mm). The deviation increases when target is far outside the focal zone (when d ranging from 2 mm to 0), reaching its maximum of 0.23 mm at the distance of 0 mm.

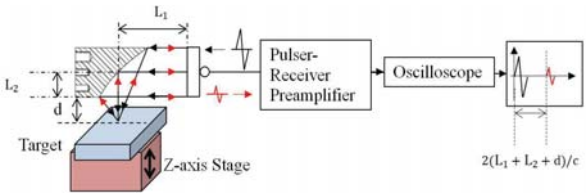

(a)

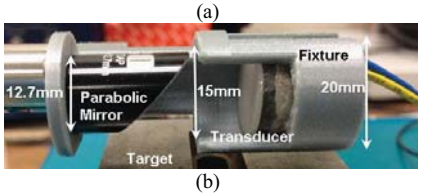

(b)

Figure 5. (a) Diagram of ultrasound distance ranging setup. (b) Photograph of transducer and parabolic mirror assembled into a 3D-printed fixture.

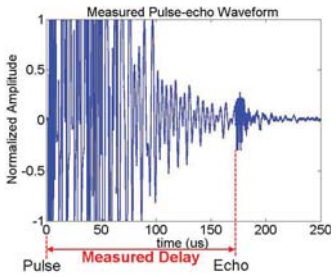

Figure 6. Captured ultrasound pulse-echo signal, showing the measured delay between "Pulse" and "Echo".

B. *Ultrasound Lateral Resolution*

To provide a good lateral resolution to resolve small targets and shapes, the ultrasound beam from the air-coupled PZT transducer has been focused with a parabolic mirror. The focused acoustic pressure field at 1 MHz has been simulated in COMSOL Multiphysics®, which shows a focal length around 6.5 mm, a focal spot around 0.7 mm and a depth of focus around 2 mm (Fig. 8).

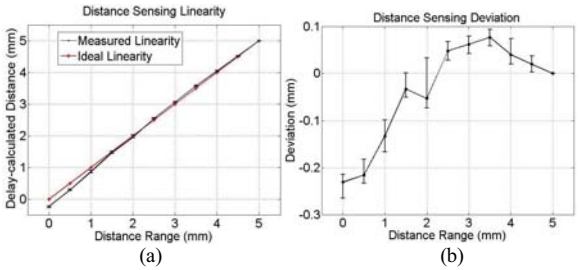

(a) (b)

Figure 7. (a) Comparison between delay-calculated (in black) and real (in red) distance. (b) Deviation of measured distance from real distance.

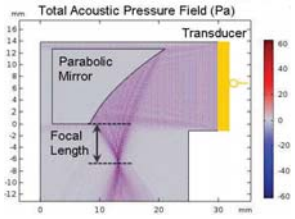

Figure 8. COMSOL simulation showing the 1 MHz ultrasound pressure field focused by the parabolic mirror.

To experimentally quantify the lateral resolution, the steel block target (Fig. 5) has been replaced with a thin copper wire with a diameter of 0.3 mm (Fig. 9), which is much smaller than the focal spot of the ultrasound beam. The copper wire has been mounted on a two-axis stage (M403.2DG, Physik Instrumente GmbH & Co. KG, Karlsruhe, Germany) at a fixed height. The profile of reflection amplitudes along the scan path has been captured and recorded by the same setup shown in Fig. 5. The FWHM value of the Gaussian-fitted profile has been used to determine the acoustic focal diameter. After repeating the linear scan at different distance (d) (from 3 mm to 7 mm), the ultrasound lateral resolution has been determined by the minimal acoustic focal diameter.

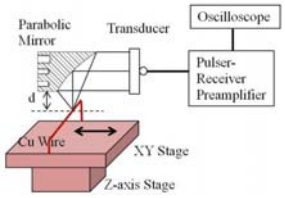

Figure 9. Diagram of lateral resolution test setup with Cu wire and 2D scanning stage.

The Cu wire has been scanned from 0 mm to 1.3 mm with 0.1 mm step at distances (d) of 3 mm, 4 mm, 5 mm, 6 mm and 7 mm. The minimum acoustic focal diameter 0.57 mm has been obtained at a distance (d) of 5 mm, which indicates an actual focal spot size of 0.57 mm and a focal length of 5 mm. The focal spot size matches with the simulation result, but the focal length is shorter than that in simulation because of larger divergence of real ultrasound beam than ideal plane wave. The Gaussian-fitted profile of reflection amplitudes across the

scanning range and the FWHM are shown in Fig. 10. The measured focal diameters at distance (d) 4 mm and 6 mm are 0.6 mm, and those at distance (d) 3 mm and 7 mm are larger than 1mm, showing the depth of focus around 2 mm, agreeing with the simulation result.

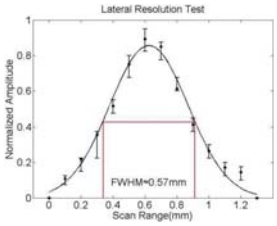

Figure 10. Ultrasound lateral resolution determined from Gaussian-fitted profile of reflection amplitudes across the scanning range at d=5 mm.

C. *Sensitivity to Shape, Area & Profile of Targets*

The sensitivity of pulse-echo ultrasound to various target shapes, areas and profiles has also been evaluated with the same setup shown in Fig. 5. The target is a 3D-printed array of circular and square elements made of Poly (lactic acid) (PLA) (Fig. 11). The circular and square elements (with diameters and side lengths from 1 mm to 5 mm) have flat, tilted, trenched, cylindrical concave, spherical concave, ridged, cylindrical convex and spherical convex profiles. Because of the limited resolution of 3D printing, all printed elements have been polished with a sand paper before testing. During the testing, the ultrasound focal spot has been aligned onto the sharp edges of the tilted elements (2nd column, from left) and the center of all other elements for data collection. The array has been

Figure 11. Diagram of 3D-printed circular and square targets in various areas and profiles.

scanned in two dimensions and the reflection amplitude of each element has been captured and recorded.

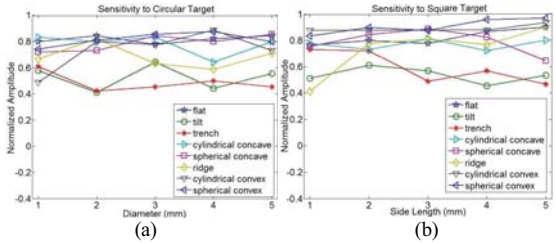

(a) (b)

Figure 12. (a) Signal amplitudes of circular targets. (b) Signal amplitudes of square targets.

Figs. 12 (a) and 12 (b) show the ultrasound reflection amplitudes from the 3D-printed circular and square elements with different areas and profiles, respectively. A general observation is that, the pulse-echo ultrasound is not sensitive to the shape, area and profile of targets, because similar reflected pulse has been received from each element, despite some differences in amplitude.

Specifically,

- Pulse-echo ultrasound is more sensitive to targets with larger area;
- Pulse-echo ultrasound is more sensitive to flat, concave, convex, ridge targets than tilted and trenched ones, for smoother surface profiles;
- Among trenched targets, pulse-echo ultrasound is more sensitive to targets in smaller area, for smoother surface profiles;
- Relatively big variations of ridge and circular cylindrical convex targets are due to the limited resolution of 3D printing and low surface uniformity after sandpaper polishing.

D. *Materials Differentiation*

The materials differentiation is based on two methods: pulse-echo ultrasound modality for porous material differentiation, and optoacoustic modality for dense solid material differentiation.

- *Porous Material Differentiation by Pulse-echo Ultrasound*

The ultrasound pulse-echo setup to differentiate porous materials is the same as that shown in Fig. 5. Polystyrene foam (high porosity, 50 mm × 25 mm × 25 mm), paper (low porosity, 0.2 mm thickness) and steel (non-porosity, 60 mm × 45 mm × 20 mm) have been placed onto Z-axis stage. To compensate the difference in their thickness, the height of Z-axis stage has been adjusted until the reflected pulses show the same delay. The amplitude of reflected pulse from foam, paper and steel at different work distance (d) has been captured and recorded.

Fig. 13 shows the amplitudes of the reflected ultrasound pulses from foam (high porosity), paper (low porosity) and steel (non-porosity) at distances (d) of 2.06 mm, 3.94 mm, 5.66 mm, and 7.37 mm, respectively. As expected, the reflection amplitude of steel is higher than that of paper, than that of foam. Therefore, the porous target materials can be differentiated from the dense solid ones by the pulse-echo ultrasound method, based on the different amplitudes of reflected pulses.

Besides porous materials, rubber and acrylic materials have been also loaded onto Z-axis stage to examine whether there are different amplitudes from steel. Unfortunately, at all four distances, the amplitudes of reflected pulses from steel, acrylic, rubber are almost the same. This indicates the limitation of pulse-echo ultrasound to differentiate dense solid materials.

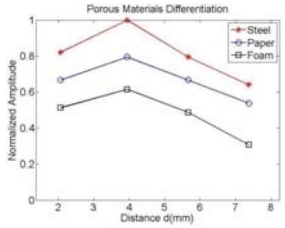

Figure 13. Porous material differentiation by pulse-echo ultrasound based on different reflection amplitudes.

- *Dense Solid Materials Differentiation by Optoacoustics*

For experimental characterization, an optoacoustic setup has been built (Fig. 14). A Q-switched 532-nm Nd:YAG laser (QL532-1W0, CrystaLaser, Reno, NV, USA) has been used as the light source. The laser pulse duration is 15~25 ns and the pulse repetition rate is 5 Hz. The pulse energy is around 50 μJ. The targets are a steel block (60 mm × 45 mm × 20 mm) coated with black ink to improve light absorption, a piece of acrylic (50 mm × 50 mm × 1.5 mm) also coated with black ink, and a piece of black rubber (70 mm × 13 mm × 21 mm). After the laser pulse illuminates the target surface (within a circular area of 2 mm in diameter), the sound induced from target propagates through air and is received by a wideband microphone (423-1139-1-ND, Digi-Key, Thief River Falls, MN, USA), amplified, recorded and averaged by 128 times. A function generator (33220A, Keysight Technologies, Santa Rosa, CA, USA) provides trigger signal for the Q-switched laser and oscilloscope. The normalized transient optoacoustic waveforms from the three targets are shown in Figure 16. The signal-to-noise voltage ratio is > 100 for steel & acrylic and ≈ 10 for rubber.

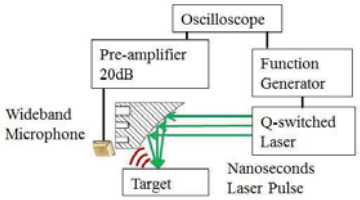

Figure 14. Diagram of dense solid materials differentiation setup with the optoacoustic method.

To show the difference between optoacoustic signals of these three materials, a classifying experiment is conducted using the open source BOSS classifier implemented by A. Bagnall et al. [25]. The classifier is trained to identify steel, rubber and acrylic, the ratio of testing data to training data is 1/3. The experimental data are transformed into BOSS histogram, serving as feature set for classification (Fig. 15). Because the BOSS histogram serves as a feature set in the classifying process, the unique symbols that only appear in one specific material will be informative for classifier. After 50 random trials, BOSS classifier gives an average accuracy of 92.8% as shown in the confusion matrix in Fig. 16. Signals from acrylic and steel can be identified with accuracy > 95%, while the possibility to misrecognize rubber as acrylic is 12%. This preliminary result demonstrates the feasibility of differentiating dense solid materials by optoacoustics.

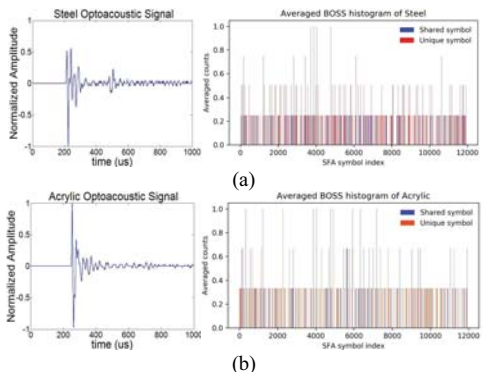

(a)

(b)

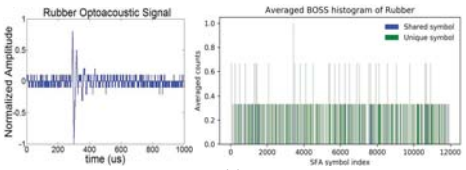

(c)

Figure 15. Optoacoustic waveform examples and averaged BOSS histogram of (a) steel (b) acrylic and (c) rubber.

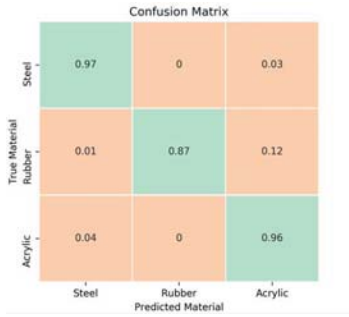

Figure 16. BOSS classifier averaged confusion matrix of steel, acrylic and rubber.

V. Conclusion and Future Work

In this paper, we have successfully demonstrated the feasibility of new acoustic and optical bi-modal distance & material sensing method for robotic grasping. It can perform distance ranging with a maximal deviation less than 0.23 mm and a lateral resolution of 0.57 mm within a 5-mm pre-touch work distance. It is capable of differentiating porous, metal, hard plastic and rubber materials before contact occurs. Pulse-echo ultrasound will firstly identify the "rough" porous category of target, and optoacoustics will secondly differentiate finer types of target materials. Therefore, this new sensing approach opens the possibility of robotic fingers for robust and nimble grasping.

To make it suitable for real applications, several issues will need to be addressed in our future work. For example, in our present setup, the material recognition and near-distance ranging are performed separately, because the transducer in use is neither hollow nor transparent. This issue can be addressed by developing an optically transparent ultrasound transducer to allow the laser to pass through. The method to address possible acoustic velocity deviations under various atmospheric conditions (pressure, humidity, etc.) will be studied. For example, the acoustic delay from a known target (e.g., a neighboring robotic finger) can be measured to determine the actual air acoustic velocity for calibration. An ultrasound receiver (covering from 10s kHz to MHz) will be developed to acquire more spectral features for more complex material identification. Ultimately, we will integrate all components into a compact package that can be built into robotic arm and fingers with automated algorithm control for scanning and mapping out target shape and material distribution before grasping.

Acknowledgment

The authors would like to thank for the inputs and feedback from Xiaoyu Duan.

REFERENCES

[1] M. T. Mason, Mechanics of Robotic Manipulation, A Bradford Book , 2001.

[2] M. Ciocarlie, K. Hsiao, E. G. Jones, S. Chitta, R. B. Rusu and I. A. Şucan, "Towards Reliable Grasping and Manipulation in Household Environments," in *Experimental Robotics, Springer Tracts in Advanced Robotics*, Berlin, Heidelberg, Springer, 2014.

[3] K. Goldberg, "Orienting Polygonal Parts Without Sensors," *Algorithmica,* vol. 10, no. 3, pp. 201-225, 1993.

[4] M. Erdmann and M. T. Mason, " An exploration of sensorless manipulation," *IEEE Journal on Robotics and Automation ,* vol. 4, no. 4, pp. 369-379, 1988.

[5] C. E. Smith and N. P. Papanikolopoulos, "Vision-Guided Robotic Grasping: Issues and Experiments," in *IEEE International Conference on Robotics and Automation (ICRA)* , Minneapolis, Minnesota, 1996.

[6] A. Wehr and U. Lohr, "Airborne laser scanning—an introduction and overview," *ISPRS Journal of photogrammetry and remote sensing,* pp. 68-82, 1999.

[7] Y. Lu, J. Lee, S.-H. Yeh, H.-M. Cheng, B. Chen and D. Song, "Sharing Heterogeneous Spatial Knowledge: Map Fusion between Asynchronous Monocular Vision and Lidar or Other Prior Inputs," in *International Symposium on Robotics Research (ISRR)*, Puerto Varas, Chile,, 2017.

[8] M.-C. Amann, T. M. Bosch, M. Lescure, R. A. Myllylae and M. Rioux, "Laser ranging: a critical review of unusual techniques for distance measurement," *Optical engineering,* vol. 40, no. 1, pp. 10-20, 2001.

[9] A. Stelzer, M. Jahn and S. Scheiblhofer, "Precise distance measurement with cooperative FMCW radar units," *Radio and Wireless Symposium, 2008 IEEE,* 2008 IEEE.

[10] K. Hsiao, P. Nangeroni, M. Huber, A. Saxena and A. Y Ng, "Reactive grasping using optical proximity sensors," *Robotics and Automation, ICRA'09. IEEE International Conference on,* pp. 2098-2105, 2009.

[11] B. Yang, P. Lancaster and J. R. Smith, "Pre-touch sensing for sequential manipulation," *Robotics and Automation (ICRA), 2017 IEEE International Conference on. IEEE,* pp. 5088-5095, 2017.

[12] J. R. Smith, E. Garcia, R. Wistort and G. Krishnamoorthy, "Electric field imaging pretouch for robotic graspers," *Intelligent Robots and Systems, 2007. IROS 2007. IEEE/RSJ International Conference on. IEEE,* pp. 676-683, 2007.

[13] B. Mayton, L. LeGrand and J. R. Smith, "An electric field pretouch system for grasping and co-manipulation," *Robotics and Automation (ICRA), 2010 IEEE International Conference on. IEEE,* pp. 831-838, 2010.

[14] C. Peng, G. Shen, Y. Zhang, Y. Li and K. Tan, "Beepbeep: a high accuracy acoustic ranging system using cots mobile devices," *Proceedings of the 5th international conference on Embedded networked sensor systems,* pp. 1-14, ACM, 2007.

[15] L. Girod and D. Estrin, "Robust range estimation using acoustic and multimodal sensing," *Intelligent Robots and Systems, 2001. Proceedings. 2001 IEEE/RSJ International Conference on,* vol. 3, IEEE, 2001.

[16] A. Elfes, "Sonar-based real-world mapping and navigation," *IEEE Journal on Robotics and Automation,* vol. 3, no. 3, pp. 249-265, 1987.

[17] R. D. Howe, "Tactile sensing and control of robotic manipulation," *Advanced Robotics,* vol. 8, no. 3, pp. 245-261, 1993.

[18] J. M. Romano, K. Hsiao, G. Niemeyer, S. Chitta and J. K. Kuchenbecker, "Human-Inspired Robotic Grasp Control With Tactile Sensing," *IEEE Transactions on Robotics,* vol. 27, no. 6, pp. 1067-1079, 2011.

[19] Q. Xu, "Design and Development of a Novel Compliant Gripper With Integrated Position and Grasping/Interaction Force Sensing," *IEEE Transactions on Automation Science and Engineering,* vol. 14, no. 3, pp. 1415 - 1428, 2017.

[20] D. A. Christensen, Ultrasonic bioinstrumentation, New York: wiley, 1988.

[21] G. Hayward and A. Gachagan, "An evaluation of 1–3 connectivity composite transducers for air-coupled ultrasonic applications," *The Journal of the Acoustical Society of America,* vol. 99, no. 4, pp. 2148-2157, 1996.

[22] T. Yano, M. Tone and A. Fukumoto, "Range finding and surface characterization using high-frequency air transducers," *IEEE transactions on ultrasonics, ferroelectrics, and frequency control,* vol. 34, no. 2, pp. 232-236, 1987.

[23] M. I. Khan and G. J. Diebold, "The photoacoustic effect generated by laser irradiation of an isotropic solid cylinder," *Ultrasonics,* vol. 34, no. 1, pp. 19-24, 1996.

[24] P. Schäfer, "The BOSS is concerned with time series classification in the presence of noise," *Data Mining and Knowledge Discovery,* vol. 29, no. 6, pp. 1505-1530, 2015.

[25] A. Bagnall, J. Lines, A. Bostrom, J. Large and E. Keogh, "The great time series classification bake off: a review and experimental evaluation of recent algorithmic advances," *Data Mining and Knowledge Discovery,* vol. 31, no. 3, pp. 606-660, 2017.

[26] T.G. Álvarez-Arenas, "Acoustic impedance matching of piezoelectric transducers to the air," *IEEE transactions on ultrasonics, ferroelectrics, and frequency control,* vol. 51, no. 5, pp. 624-633, 2004.

[27] [Online]. Available: https://grabcad.com/library/tactile-sensing-robotic-finger.

[28] [Online]. Available: http://www.thermalps.com.au/imagesDB/wysiwyg/TD

S_Expanded_Polystyrene.pdf.

[29] [Online]. Available: https://mysite.du.edu/~jcalvert/waves/soundwav.htm.

[30] [Online]. Available: https://www.paperonweb.com/density.htm.

[31] [Online]. Available: https://www.engineeringtoolbox.com/density-solids-d_1265.html.

[32] [Online]. Available: https://www.engineeringtoolbox.com/young-modulus-d_417.html.

[33] [Online]. Available: https://www.engineeringtoolbox.com/linear-expansion-coefficients-d_95.html.

[34] [Online]. Available: https://www.engineeringtoolbox.com/specific-heat-capacity-d_391.html.

[35] [Online]. Available: http://www.matweb.com/search/DataSheet.aspx?MatGUID=a5e93a1f1fff43bcbac5b6ca51b8981f& ckck=1.